Scientific paper

Crystal Structure Analysis and Anticancer Potential of a Naphthalene-Based Schiff Base Against Breast Cancer

Tolga Göktürk,¹ Turan Demircan,^{2,*} Tuncer Hökelek,³ Mervenur Yavuz,⁴ Ramazan Güp,¹ Cansu Topkaya^{1,*}

¹ Mugla Sitki Kocman University, Department of Chemistry, 48100, Mentese, Muğla, Türkiye

² Mugla Sitki Kocman University, Department of Medical Biology, 48100, Menteşe, Muğla, Türkiye

³ Hacettepe University, Department of Physics, 06800 Beytepe-Ankara, Türkiye

⁴ Mugla Sitki Kocman University, Institute of Natural Sciences, Department of Molecular Biology and Genetics, 48100, Menteşe, Muğla, Türkiye

* Corresponding author: E-mail: cansutopkaya@mu.edu.tr; turandemircan@mu.edu.tr

Received: 02-04-2025

Abstract

The crystal structure of the Schiff base compound 4-hydroxy-*N*-[(1*Z*)-1-(naphthalen-2-yl)ethylidene]benzohydrazide was determined using X-ray diffraction analysis, confirming the molecular structure previously inferred from spectroscopic data. The molecule exhibits nearly planar rings with specific dihedral angles. The crystal structure features intermolecular O–H···O and N–H···O hydrogen bonds that form a two-dimensional network, significantly stabilizing the structure. Hirshfeld surface analysis identified key intermolecular interactions, with notable contributions from H···C/C···H and H···H contacts. Energy calculations highlighted the dominant role of electrostatic interactions in the overall stability of the crystal. *In vitro* studies identified significant anticancer effects, with IC₅₀ values of 38 μM for MCF7 cells and 57 μM for MDA-MB-231 cells, demonstrating dose-dependent inhibition of cell viability, migration, and clonogenic growth. *In silico* analyses revealed a strong binding affinity to ERRγ and predicted favorable oral bioavailability. KEGG pathway enrichment analysis of the predicted targets indicated their significant involvement in cancer-related pathways. The combined structural, *in vitro*, and *in silico* analyses provide a comprehensive understanding of the compound's properties, laying a strong foundation for future preclinical and clinical studies.

Keywords: Crystal structure, naphthalene, Schiff base, breast cancer, MCF7

1. Introduction

Schiff base compounds possess an azomethine functional group (-HC=N-),¹ which grants them diverse biological and pharmaceutical properties. This has made them increasingly valuable in the discovery of effective, active and safe therapeutic agents in drug design. These compounds interact with specific regions of DNA strands and function as antifungal,² antioxidant, antibacterial³-5 and antitumor agents. Additionally, Schiff bases, as chelating ligands containing heteroatoms, exhibit extensive biological activities, and are employed in various applications.

Compounds containing a naphthyl ring hold significant importance in pharmacological research, particularly for their antitumor activities and other biological functions. 8,9 The naphthyl ring enhances lipophilicity, facilitating passage through biological membranes and interactions with target biomolecules. Such compounds have demonstrated high efficacy against various cancer cell lines. For example, benzimidazole derivatives with a naphthyl ring have shown potent anticancer activity against MCF-7 (breast cancer), A549 (lung cancer), and SW480 (colon cancer) cell lines. Therefore, naphthyl ring-containing compounds, particularly Schiff base compounds, represent promising targets in drug development processes due to their significant antitumor potential.

Based on this information, the crystal structure of the previously synthesized and characterized Schiff base compound 4-hydroxy-N-[(1Z)-1-(naphthalen-2-yl)ethylidene] benzohydrazide (TC2), ¹⁰ has been elucidated for the first

time in this study. Additionally, Hirshfeld surface analysis, interaction energy calculations and energy frameworks of the compound are presented. Furthermore, the biological efficacy of the naphthyl-containing Schiff base was evaluated through *in vitro* tests on MCF7 and MDA-MB-231 cancer cell lines. Our data demonstrated that treatment with TC2 significantly suppressed carcinogenic activity, consistent with the findings of *in silico* analyses.

2. Experimental

2. 1. X-Ray Crystallography

The crystallographic data of the title compound, were collected on a Bruker APEX II QUAZAR three-circle diffractometer using Mo K_{α} radiation ($\lambda = 0.71073 \text{ Å}$) at 273(2) K. The data were processed by SHELX program packages (SHELXT 2018/211 and SHELXL2018/312) for solving and refining the structure, and ORTEP-313 and PLATON¹⁴ programs were used in drawings. The NH (H2A) and OH (H2B) hydrogens were located in a difference Fourier map and refined isotropically, while the remaining hydrogen atom positions were calculated geometrically at distances of 0.93 Å (for aromatic CH) and 0.96 Å (for CH₃), and refined using a riding model by applying the constraints of $U_{iso}(H) = kU_{eq}(C)$, where k = 1.2 for aromatic CH and k = 1.5 for methyl hydrogen atoms. Crystallographic data for the structure reported herein have been deposited with the Cambridge Crystallographic Data Centre as Supporting Information (CCDC No. 2368040). Copies of the data can be obtained through application to CCDC, 12 Union Road, Cambridge CB2 1EZ, UK. (fax: +44 1223 336033 or e-mail: deposit@ccdc.cam.ac.uk or at http://www.ccdc.cam.ac.uk).

2. 2. In Vitro Studies

The experimental steps for the *in-vitro* studies were detailed elsewhere, ^{15,16} and the protocols from these studies were adopted for the current investigation. All experiments were performed in triplicate.

Briefly, breast cancer cell lines MCF-7 and MDA-MB-231 were sourced from our own stocks. The cells were cultured in Dulbecco's Modified Eagle's Medium (DMEM), supplemented with 10% fetal bovine serum (FBS) and 1% penicillin/streptomycin. They were incubated at 37°C in a humidified cell culture incubator with 5% CO₂. Cell passaging was performed once the cells reached 80% confluency. Cell proliferation was routinely monitored using an inverted microscope. TC2 was dissolved in dimethyl sulfoxide (DMSO) to prepare stock solutions, which were subsequently diluted in complete culture medium to achieve the desired concentrations for the assays.

Cell viability was assessed using the CellTiter 96* Non-Radioactive Cell Proliferation Assay Kit according to the manufacturer's protocol, with absorbance measured at

570 nm. IC₅₀ values were calculated by fitting dose-response curves using the 'drc' package¹⁷ in the R programming language. The colony formation assay (CFA) was employed to assess the ability of cells to form colonies following HL1 exposure. Cells were fixed with 100% methanol for 20 min at room temperature, stained with 0.2% Crystal Violet for 15 min, washed twice with ddH₂O to remove background staining, and the plates were left to dry. Digital images were captured using a bright-field microscope. A spheroid formation assay (SFA) was conducted to evaluate the growth of breast cancer cells without attachment to a surface, with cells incubated for 30 days following established protocols. The in vitro wound healing assay (WHA) assessed cell migration in response to TC2 treatment, with digital images taken at 0 and 24 h after wound creation.

The apoptotic effects of TC2 on MCF-7 cells were evaluated using the Alexa Fluor® 488 Annexin V/Dead Cell Apoptosis kit and analyzed by flow cytometry (BD Accuri™ C6 Plus). Reactive oxygen species (ROS) levels were assessed using the CellROX™ Green Flow Cytometry Assay Kit following the manufacturer's instructions and analyzed by flow cytometry. Mitochondrial membrane potential (MMP) was measured to evaluate mitochondrial function and integrity using the Mitochondrial Membrane Potential Assay Kit (with JC-1) according to the producer's procedure, with analysis by flow cytometry (BD Accuri™ C6 Plus) under green fluorescence emission. To investigate the molecular mechanisms underlying TC2's cellular effects, quantitative reverse transcription PCR (qRT-PCR) was performed on a panel of proto-oncogenes and tumor suppressor genes. Data were analyzed using the $2-\Delta\Delta Ct$ method and relative expression data were visualized on a bar chart using the 'ggplot2' package in the R environment.

2. 3. In Silico Studies

For chemoinformatics analysis, TC2 potential targets were predicted using the Swiss target prediction tool.¹⁸ A combination of 2D and 3D similarity evaluations generated a list of predicted proteins, which were then subjected to Kyoto Encyclopedia of Genes and Genomes (KEGG) enrichment analysis using the 'ClusterProfiler' package¹⁹ in the R environment. The top 20 KEGG pathways were illustrated in a dot plot using the 'ggplot2' package in R, as described elsewhere.²⁰ The highest-scoring predicted target protein, Estrogen-Related Receptor Gamma (ERRy), was used for molecular docking studies. Molecular interaction studies between ERRy (PDB ID: 2GPP) and TC2 were conducted using the Mcule drug discovery platform²¹ and SwissDock.²² Both analyses followed an automated docking protocol, which included SMILES input conversion to 2D MOL by indigo, conversion of ligand 2D MOL to 3D MOL by OpenBabel, conversion of ligand 3D MOL to PDBQT by AutoDock tools and docking by AutoDock Vina with default parameters. The mean ΔG values from the selected docking tools were used to reach a consensus. Absorption, Distribution, Metabolism and Excretion (ADME) profiling and *in silico* toxicity studies were performed using SwissADME¹⁸ and ProTox-II²³ tools, using the SMILES code. SwissADME predicts pharmacokinetics and drug-likeness through molecular similarity and predictive regression analyses.

The supplementary file contains detailed descriptions and additional information regarding the interaction energy calculations and energy frameworks.^{24–27}

3. Results and Discussion

3. 1. X-Ray Structure

The synthesis of 4-hydroxy-N-[(1Z)-1-(naphthalen-2-yl)ethylidene]benzohydrazide (TC2) was carried out following a previously reported method. 10 The X-ray crystal structure determination of the TC2 confirms its structural assignment based on spectroscopic data. Experimental parameters are summarized in Table 1, while the hydrogen bond geometry and selected interatomic distances are provided in Tables 2 and 3, respectively. The molecular structure along with the atom-numbering scheme is depicted in Fig. 1. The planar rings A (C1-C6), B (C10-C13/C18/C19) and C (C13-C18) exhibit dihedral angles of A/B = $6.45(7)^{\circ}$, A/C = $5.59(8)^{\circ}$ and B/C = 0.99(8)°. Atoms O2, C7 and C8, C9 are 0.0436(23) Å, 0.0283(26) Å and 0.0530(26) Å, -0.0389(29) Å away from the best least-squares planes of the adjacent rings, respectively. This indicates that these atoms are nearly coplanar with their corresponding ring planes.

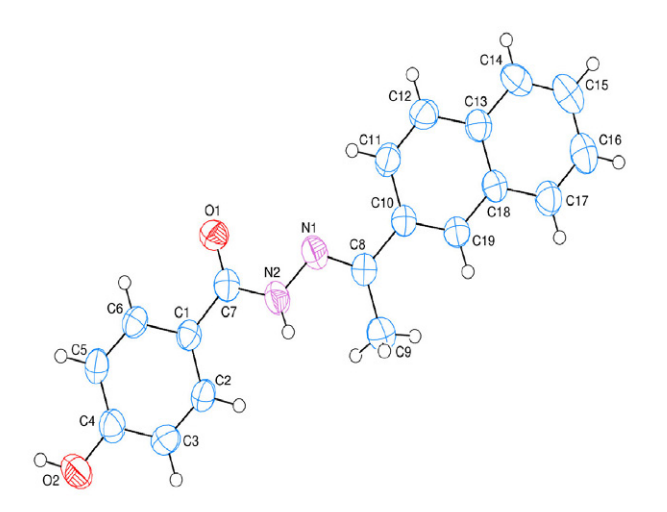


Figure 1. The asymmetric unit of the title compound with the atom numbering scheme. Thermal ellipsoids are drawn at the 50% probability level.

In the crystal structure, the intermolecular O-H···O and N-H···O hydrogen bonds link the molecules, enclosing $R_4^4(22)$ ring motifs, into a network structure almost

Table 1. Experimental details.

Chemical formula	$C_{19}H_{16}N_2O_2$	
M_r	304.34	
Crystal colour, habit	Colourless, block	
Crystal system	Orthorhombic	
Space group	$P 2_1 2_1 2_1$	
a (Å)	6.1227(4)	
b (Å)	12.5222(3)	
c (Å)	20.3948(5)	
$V(Å^3)$	1563.66(12)	
Z	4	
$D_{\rm calc}$ (g cm ⁻³)	1.293	
μ (mm ⁻¹)	0.09	
F(000)	640	
Number of unique data	3162	
Number of observed data $[I > 2\sigma(I)]$	1782	
Number of parameters	217	
Number of restraints	2	
R_1 , wR_2 $[I > 2\sigma(I)]$	0.0503, 0.0908	
R_1 , wR_2 (all data)	0.1243, 0.1137	
Goodness of fit on F^2	1.027	

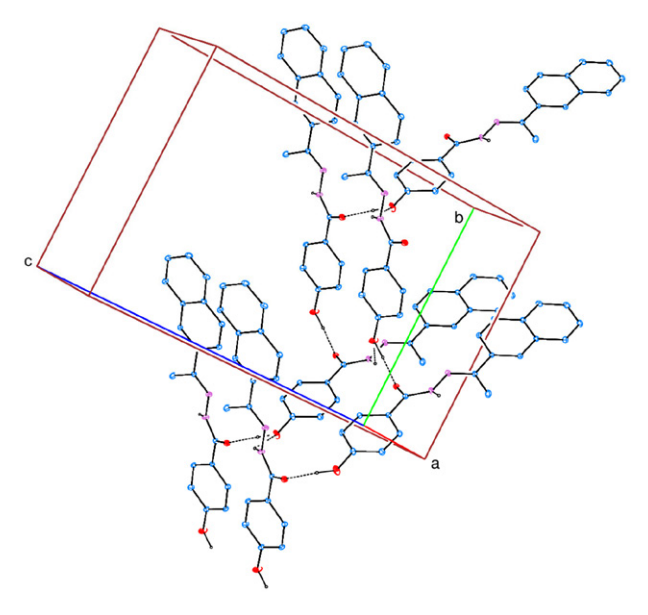


Figure 2. A partial packing diagram. The intermolecular O–H···O and N–H···O hydrogen bonds are shown as dashed lines. The other H atoms have been omitted for clarity.

parallel to the bc-plane (Fig. 2), in which they may be effective in the stabilization of the structure. There is not any $\pi \cdots \pi$ interaction. But, three weak C–H··· π interactions (Table 2) are observed.

3. 2. Hirshfeld Surface Analysis

In order to visualize the intermolecular interactions in the crystal of the title compound, a Hirshfeld surface (HS) analysis^{29,30} was carried out by using *Crystal Explorer* 17.5.²⁴ In the HS plotted over d_{norm} (Fig. 3), the white sur-

face indicates contacts with distances equal to the sum of van der Waals radii, and the red and blue colours indicate distances shorter (in close contact) or longer (distinct contact) than the van der Waals radii, respectively.³¹

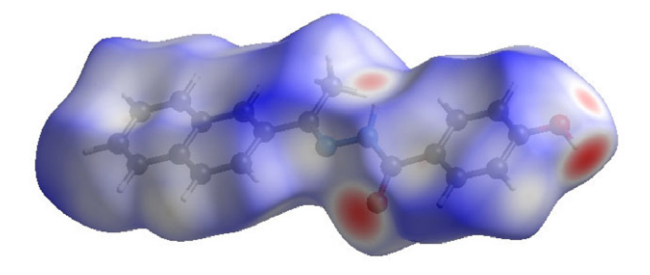


Figure 3. View of the 3D HS of the title compound plotted over d_{norm} in the range of -0.7629 to 1.4816 a.u

The bright-red spots also correspond to positive electrostatic potential (blue regions, associated with H-bond donors) and to negative electrostatic potential (red regions, associated with H-bond acceptors) on HS mapped over the electrostatic potential, ^{28,32} as shown in Fig. 4.

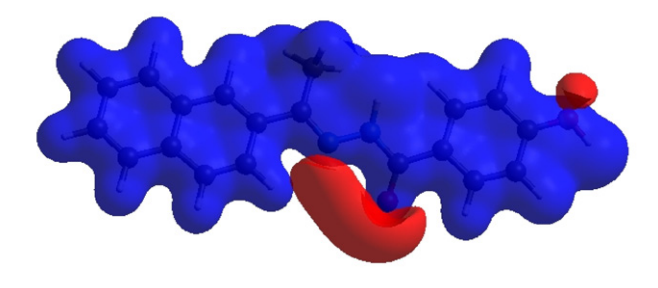


Figure 4. View of the 3D HS of the title compound plotted over electrostatic potential energy in the range -0.0500 to 0.0500 a.u. using the STO-3 G basis set at the Hartree–Fock level of theory.

The $\pi\cdots\pi$ stacking and C-H··· π interactions were evaluated using the shape-index tool. This surface analysis technique is particularly effective for identifying characteristic packing patterns, such as planar stacking arrangements and aromatic interactions, including C-H··· π and π ··· π interactions. In the shape index representation, π ··· π stacking interactions are indicated by the presence of adja-

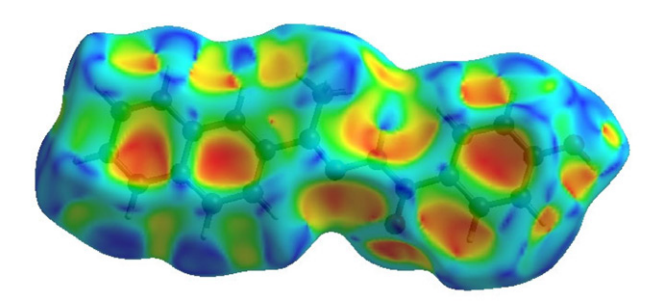


Figure 5. HS of the title compound plotted over shape-index.

cent red and blue triangles. Conversely, the absence of adjacent red or blue triangles signifies a lack of π ··· π interactions.

Fig. 5 clearly suggests that there are no π ··· π interactions in title compound. However, the shape index highlights C–H··· π interactions as "red p-holes", corresponding to electron ring interactions between CH groups and the centroids of aromatic rings in neighboring molecules (Table 2, Fig. 5). The overall 2D fingerprint plot (Fig. 6a) and those delineated into H...C/C...H, H...H, H...O/O...H, H...N/N...H, C...C, C...O/O...C and N...O/O...N contacts³³ are illustrated in Figs. 6 b–h respectively, along with their respective contributions to the HS.

C–H... π interactions contribute significantly to crystal packing, with H...C/C...H (Table 3, Fig. 6b), accounting for 39.8%. These appear as characteristic wing-like features with tips at $d_{\rm e}+d_{\rm i}=2.66$ Å. H...H contacts (Table 3, Fig. 6c) are viewed as the widely scattered points of high density due to the large hydrogen content of the molecule with the tip at $d_{\rm e}=d_{\rm i}=1.17$ Å.

H...O/O...H contacts (15.7%, Table 3, Fig. 6d), are represented by pair of spikes $d_{\rm e}+d_{\rm i}=1.60$ Å, while H...N/N...H contacts (6.1%, Table 3, Fig. 6e), exhibit symmetric distributions with tips at $d_{\rm e}+d_{\rm i}=2.58$ Å. The contributions of C...C (0.7%, Fig. 6f), C...O/O...C (0.7%, Fig. 6g) and N...O/O...N (0.1%, Fig. 6h) contacts to the crystal packing, appearing as scattered low-density points on the fingerprint plots.

Table 2. Hydrogen-bond geometry (Å, °)

D—H···A	D—H	H···A	DA	D—H···A
N2-H2A···O2 ⁱⁱ	0.87(2)	2.37(3)	3.028(3)	132(3)
O2-H2B···O1i	0.99(3)	1.62(3)	2.610(3)	175(3)
C3-H3···Cg3i	0.93	2.87	3.502(3)	129
C12-H12···Cg3 ^{iv}	0.93	2.80	3.475(3)	130
C17-H17···Cg1 ⁱ	0.93	2.84	3.582(3)	137

Symmetry codes: (i) -x, -y + 1, -z + 1; (ii) -x + 1, $y + \frac{1}{2}$, $-z + \frac{1}{2}$.

The HS representations with the function d_{norm} plotted onto the surface are shown for the H...C/C...H, H...H and H...O/O...H interactions in Figs. 7a–c, respectively.

The HS analysis highlights the importance of H-atom contacts in crystal packing. The abundance of H...C/C...H, H...H and H...O/O...H interactions indicates the significance of van der Waals forces and hydrogen bonding as the primary contributors to the crystal packing.³⁴

3. 3. Interaction Energy Calculations and Energy frameworks

Hydrogen-bonding interaction energies (in kJ mol⁻¹) are -22.9 ($E_{\rm ele}$), -6.9 ($E_{\rm pol}$), -34.2 ($E_{\rm dis}$), 18.3 ($E_{\rm rep}$) and -47.8 ($E_{\rm tot}$) (for O2–H2B···O1) and -64.6 ($E_{\rm ele}$), -15.6

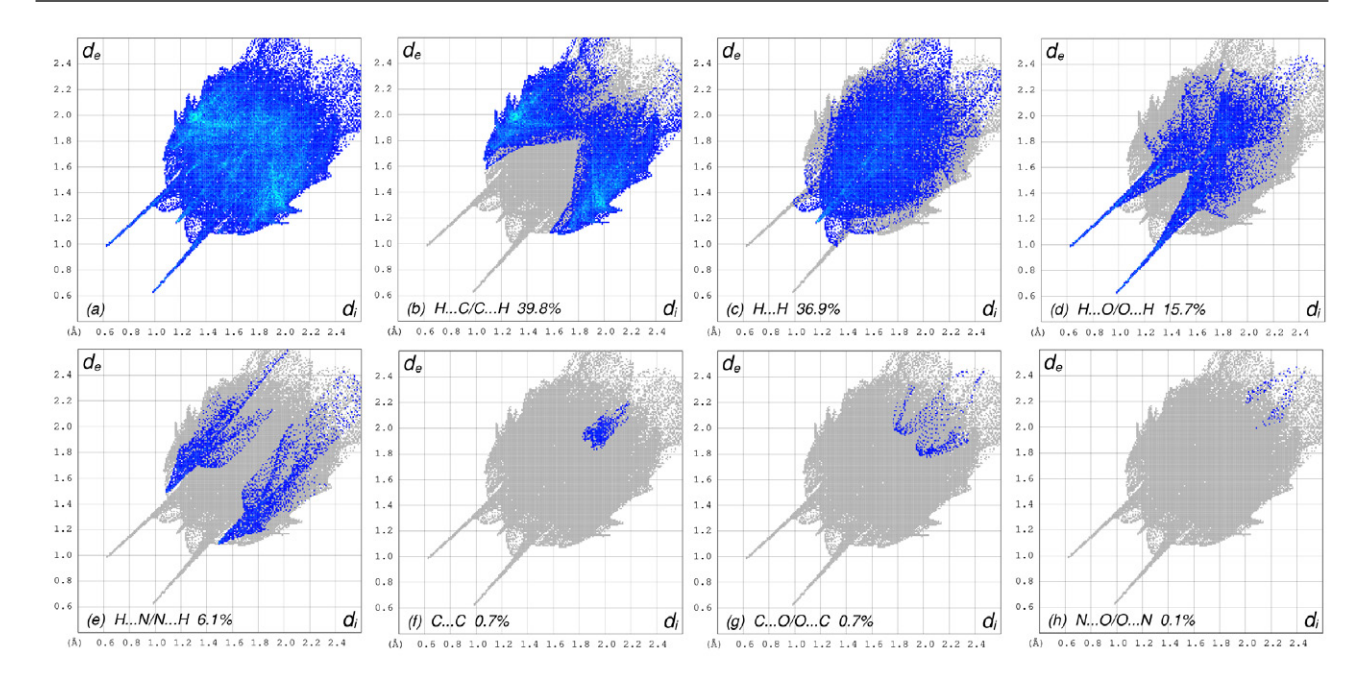


Figure 6. The full 2D fingerprint plots for the title compound, showing (a) all interactions, and delineated into (b) H...C/C...H, (c) H...H, (d) H...O/O...H, (e) H...N/N...H, (f) C...C, (g) C...O/O...C and (h) N...O/O...N interactions. The d_i and d_e values are the closest internal and external distances (in Å) from given points on the HS contacts.

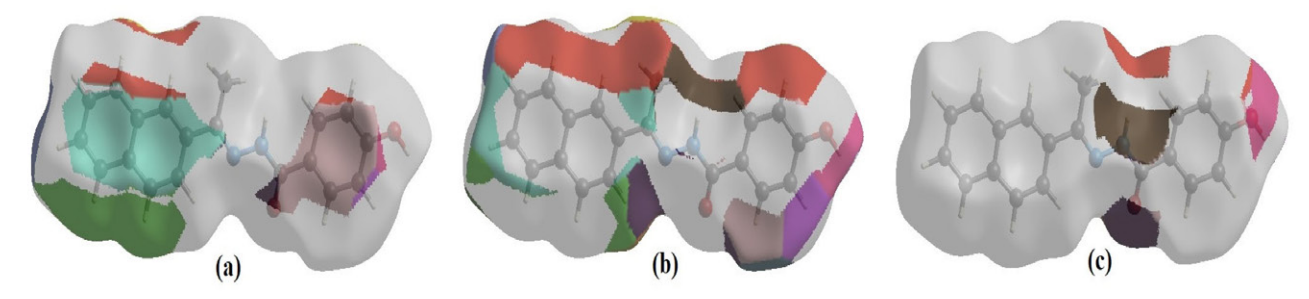


Figure 7. The HS representations with the function dnorm plotted onto the surface for (a) H...C/C...H, (b) H...H and (b) H...O/O...H interactions.

 $(E_{\rm pol})$, -18.3 $(E_{\rm dis})$, 79.9 $(E_{\rm rep})$ and -46.4 $(E_{\rm tot})$ (for N2–H2A···O2). Also, energy frameworks were visualized for electrostatic (red cylinders), dispersion (green cylinders), and total (blue cylinders) energies (Fig. 8). Analysis of these frameworks reveals that the electrostatic energy is the primary factor stabilizing the structure.

3. 4. In vitro and in silico Analyses

The IC $_{50}$ of TC2 was determined to be 38 μ M for MCF7 cells and 57 μ M for MDA-MB-231 cells, suggesting that MCF7 cells exhibit greater sensitivity to TC2 treatment. The relative viability of MCF7 cells decreased in a dose-dependent manner with TC2 treatment, as follows:

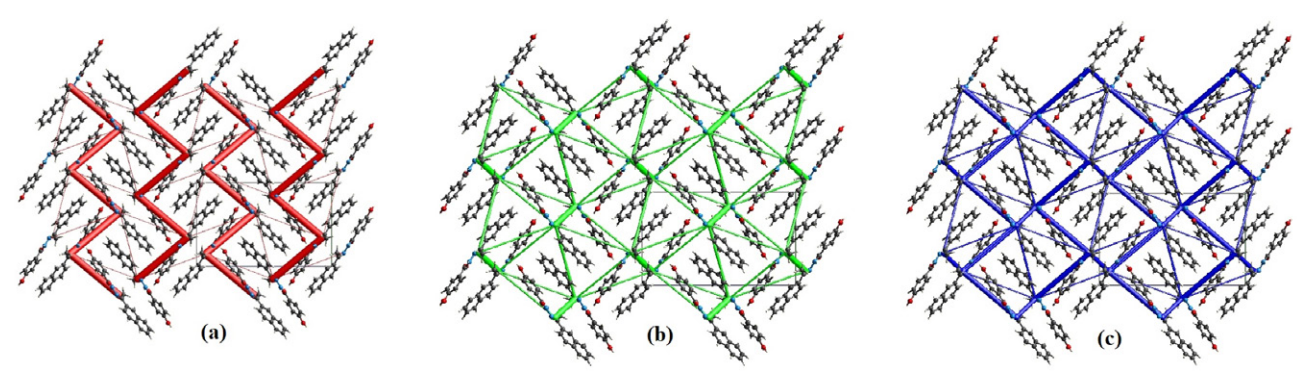


Figure 8. The energy frameworks for a cluster of molecules of the title compound, viewed down the a-axis, showing: (a) E_{ele} , (b) E_{dis} and (c) E_{tot} diagrams.

97% at 0.0001 mM, 94% at 0.001 mM, 78% at 0.01 mM, 34% at 0.05 mM, 11% at 0.1 mM and 2% at 0.5 mM. For MDA-MB-231 cells, relative viability was recorded as 95% at 0.0001 mM, 91% at 0.001 mM, 84% at 0.01 mM, 58% at 0.05 mM, 17% at 0.1 mM and 9% at 0.5 mM. These findings indicate a substantial decrease in cell viability with increasing concentrations of TC2, demonstrating its potent anticancer effects on MCF7 and MDA-MB-231 cell lines (Fig. 9a).

CFA and SFA provided further evidence of TC2's inhibitory properties at its IC_{50} concentrations. In the CFA, TC2 treatment significantly decreased colony formation in both cell lines, highlighting its negative effect on clonogenic survival. Likewise, the SFA showed a substantial reduction in spheroid development, indicating that TC2 effectively restricts three-dimensional cell proliferation. Collectively, these results demonstrate the potent inhibitory effects of TC2 in both 2D and 3D cell culture models (Fig. 9b).

The WHA results revealed the impact of TC2 on cell migration. After 24 hours, the relative wound area in control group of MCF7 cells reduced to 22%, reflecting significant wound closure. In contrast, TC2-treated MCF7 cells retained a relative wound area of 78%, indicating a pro-

nounced inhibition of cell migration. Similarly, in MDA-MB-231 cells, the control group showed a reduction in the relative wound area to 22%, whereas TC2 treatment resulted in a relative wound area of 75%, emphasizing TC2's strong inhibitory effect on migration. These findings demonstrate that TC2 markedly reduces the migratory ability of both MCF7 and MDA-MB-231 cells (p < 0.001) (Fig. 9c).

Due to the lower IC $_{50}$ value for MCF7 compared to MDA-MB-231, we decided to conduct in-depth cellular and molecular analyses using MCF7 cells. TC2 treatment significantly enhanced the rate of apoptosis in these cells. Flow cytometry analysis using Annexin V/7AAD staining demonstrated an increase in apoptotic cells from 7% in the control group to 18.7% in the TC2-treated group, representing a 2.7-fold rise. This substantial increase highlights the pro-apoptotic effect of TC2 on MCF7 cells (p < 0.001) (Fig. 10a).

MMP analysis further corroborated the induction of apoptosis by TC2. Flow cytometry data showed a significant shift in the number of cells exhibiting higher fluorescence values, indicative of altered mitochondrial function. Specifically, the proportion of cells with lower MMP increased from 3.6% in the control group to 17.2% in the

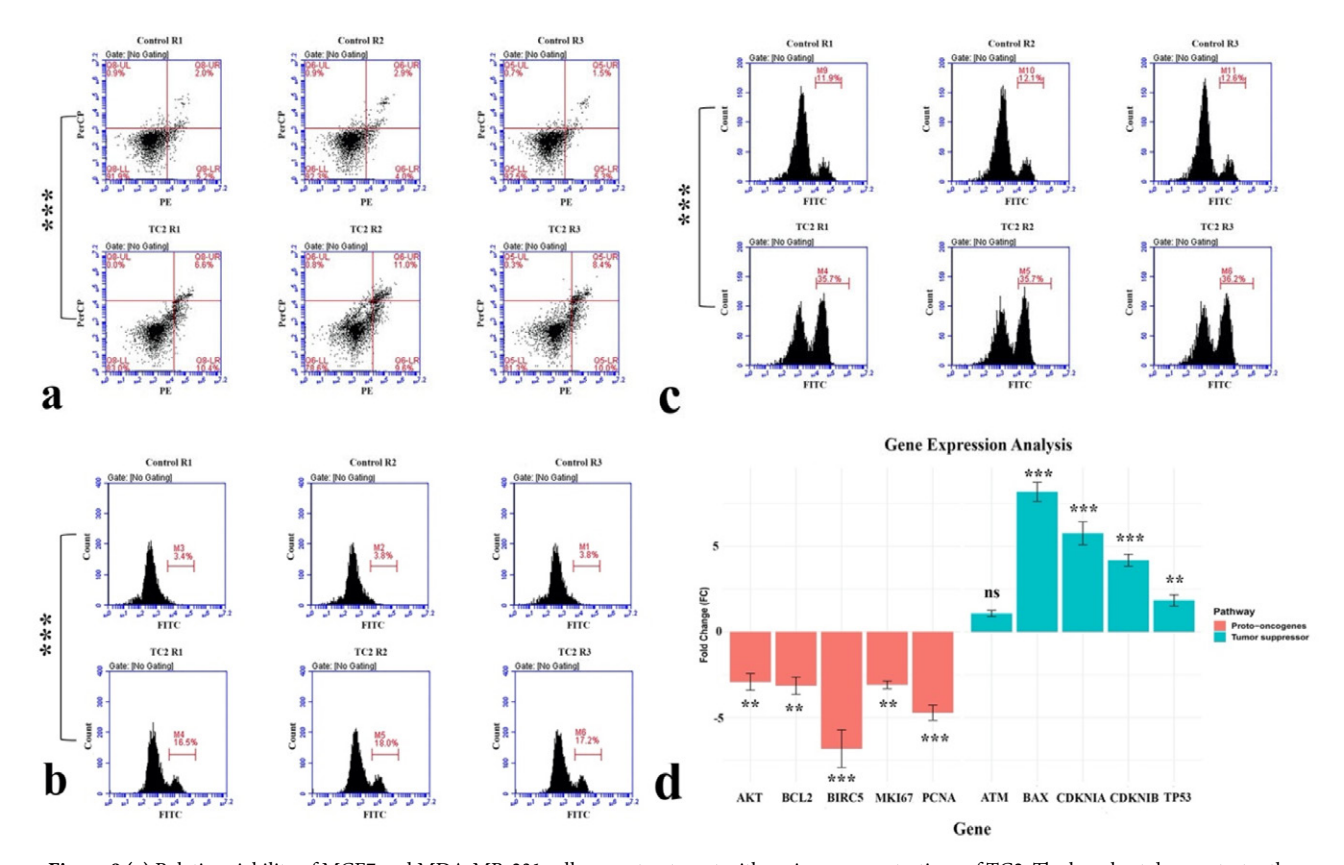


Figure 9 (a) Relative viability of MCF7 and MDA-MB-231 cells upon treatment with various concentrations of TC2. The bar chart demonstrates the dose-dependent anti-carcinogenic effects of TC2 on cell viability. (b) Colony formation assay (Top panel) of MCF7 and MDA-MB-231 cells treated with IC $_{50}$ dose of TC2. The assay illustrates the impact of TC2 on the ability of these cells to form colonies. Spheroid formation assay (Bottom panel) showing the effect of TC2 on the 3D growth of MCF7 and MDA-MB-231 cell spheroids. (c) Wound healing assay indicating the migration ability of MCF7 and MDA-MB-231 cells post-TC2 treatment. The assay results highlight the inhibitory effects of TC2 on cell migration and wound closure over 24 h. ***p < 0.001, **p < 0.01, ns; non-significant. h; hours.

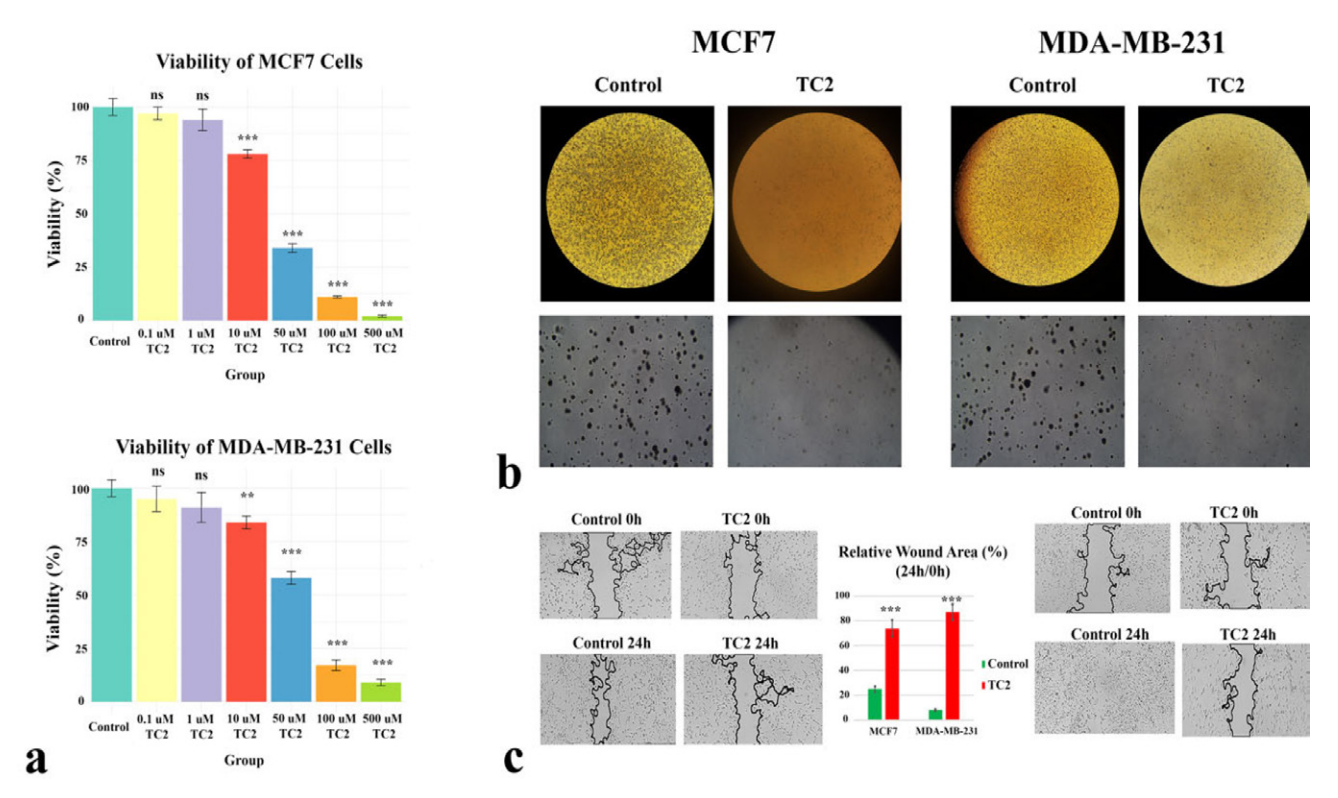


Figure 10 (a) Flow cytometry analysis using Annexin V/7AAD staining showing the apoptosis rate in MCF7 cells. The data compares the percentage of apoptotic cells between control and TC2-treated groups, demonstrating the pro-apoptotic effect of TC2. (b) MMP staining and flow cytometry analysis for MCF7 cells. The figure presents the MMP status in both control and TC2-treated cells, indicating the impact of TC2 on mitochondrial health and function. (c) Flow cytometry is applied to measure the ROS levels in MCF7 cells. The panel illustrates the ROS production in control versus TC2-treated cells, highlighting the oxidative stress induced by TC2 treatment. (d) Relative gene expression analysis by qPCR for several tumor suppressor and proto-oncogenes in MCF7 cells. The bar graph compares the expression levels of key genes in control and TC2-treated groups, show-casing the regulatory effects of TC2 on gene expression related to tumor suppression and oncogenesis. ***p < 0.001, **p < 0.01, ns; non-significant, MMP; Mitochondrial membrane potential.

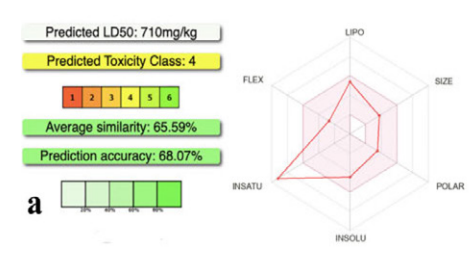
TC2-treated group. This increase in cells with compromised MMP supports the observed rise in apoptosis rates, highlighting the impact of TC2 on mitochondrial integrity and cell viability (Fig. 10b). Consistently, the production of ROS was markedly elevated in MCF7 cells treated with TC2. Flow cytometry analysis revealed that ROS levels were approximately three times higher in TC2-treated cells compared to control cells. This significant increase in ROS production indicates that TC2 induces oxidative stress, contributing to its anti-carcinogenic effects (Fig. 10c).

Next, gene expression analysis was carried out, and qRT-PCR results provided additional insights into the molecular mechanisms underlying TC2's effects. A significant decrease was observed in the expression of proto-oncogenes AKT, BCL2, BIRC5, MKI67, and PCNA. Concordantly, there was a significant increase in the expression of tumor suppressor genes BAX, CDKN1A, CDKN1B, and TP53. These changes in gene expression profiles indicate that TC2 not only inhibits oncogenic pathways but also enhances tumor suppressor pathways, thereby contributing to its overall anti-carcinogenic activity (Fig. 10d).

We also performed *in silico* analyses to predict the potential cellular interactors of TC2 and the pathways en-

riched by these interactors. The molecular docking analysis revealed a binding free energy of -10.6 kcal/mol between the ligand TC2 and the protein (ERRy) encoded by the ESRRG gene (Fig. 11a). This low binding free energy indicates a strong and stable interaction, suggesting that TC2 may effectively bind to ERRy. ERRy is an orphan nuclear receptor involved in various biological processes. It is known to play crucial roles in the regulation of energy homeostasis, mitochondrial biogenesis, and oxidative metabolism.35 In the context of breast cancer, ERRy has been implicated in the modulation of cellular proliferation and differentiation, and it has been shown that ERRy enhances estrogen response element-driven transcription in MCF-7 cells.³⁶ Moreover, previous studies have shown that ERRy promotes resistance to Tamoxifen in estrogen receptor-positive (ER+) breast cancer models and that its transcriptional activity is influenced by the activation of the ERK/MAPK pathway.³⁷ When ERRγ is hyper-activated or over-expressed, it initiates a pro-survival transcriptional program, thereby enhancing the aggressiveness of ER+ breast cancer growth.³⁸ Therefore, key functions of ERRy in breast cancer development make it a crucial target for therapeutic interventions. It is plausible to suggest that the observed anti-carcinogenic effect of TC2 may be partially





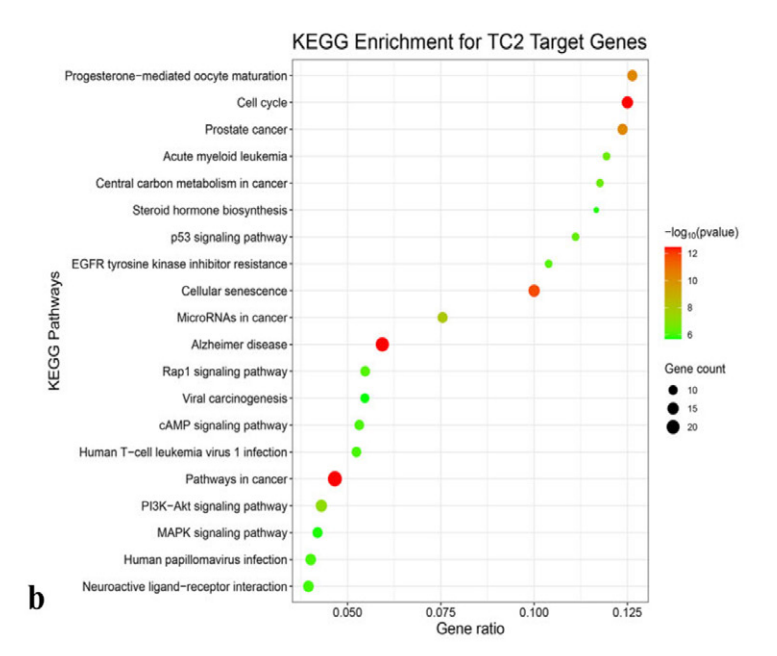


Figure 11. (a) The upper panel displays the molecular docking result which demonstrates a successful binding interaction between TC2 and ERRγ (PDB ID: 2GPP). The second panel presents the results from the Tox-Pro II analysis, which predicts toxicity profile of TC2. The third panel is a radar plot generated by SwissADME, illustrating the pharmacochemical properties of TC2. The radar plot visualizes several critical attributes such as lipophilicity, solubility, size, polarity, flexibility, and synthetic accessibility. (b) The panel displays a dot plot of top 20 KEGG pathways enriched by the target genes of TC2. The size of each bubble correlates with the gene count for the corresponding pathway, indicating the number of target genes involved in each pathway. The color gradient of the bubbles, ranging from green to red, represents the −log(10) *p*-value, with increasing significance as the color transitions to red.

mediated through the inactivation of ERRγ, which should be explored in future studies.

The ADME analysis of TC2 predicted an LD $_{50}$ (lethal dose for 50% of the population) of 710 mg/kg, categorizing it within toxicity class 4 (Fig. 11b). This classification indicates that TC2 has a relatively low acute toxicity, suggesting a favorable safety profile for further development. The radar plot generated by SwissADME demonstrated that most of TC2's physicochemical properties fall within the suitable range for oral bioavailability (Fig. 11b). These properties include lipophilicity, solubility, size, polarity, flexibility, and synthetic accessibility, which collectively support the potential of TC2 as an orally administrable drug.

Cancer-related KEGG pathways were significantly enriched by the the predicted targets of TC2 (Fig. 11c). Among the top 20 enriched pathways, several are particularly noteworthy including 'cell cycle', 'Prostate Cancer', 'Pathways in Cancer', 'Cellular Senescence', and 'miRNAs in cancer'. Enrichment of these pathways indicates potential mechanisms through which TC2 may exert anticancer effects. The enrichment of these pathways highlights the potential of TC2 to influence critical biological processes associated with cancer development and progression. These findings, combined with the molecular docking results and favorable ADME properties, establish TC2 as a compelling candidate for further exploration in cancer therapeutics, particularly for targeting pathways associat-

ed with cell cycle regulation and tumor suppression.

4. Conclusions

We present a comprehensive evaluation of TC2, a naphthalene-based Schiff base, through a combination of crystallographic, *in vitro*, and *in silico* investigations. X-ray diffraction analysis confirmed that TC2 exhibits nearly planar ring systems and forms a robust two-dimensional hydrogen bonding network, with energy framework calculations indicating that electrostatic interactions play a critical role in maintaining the crystal structure. Complementary Hirshfeld surface analysis revealed significant contributions from H····C/C···H (39.8%) and H···H (15.7%) contacts.

In vitro studies demonstrated that TC2 exerts potent anticancer activity, with IC $_{50}$ values of 38 μ M for MCF7 cells and 57 μ M for MDA-MB-231 cells. The compound effectively inhibited cell migration, colony formation, and spheroid growth, suggesting a strong antiproliferative effect. In parallel, in silico docking analysis revealed a strong binding affinity to ERR γ (–10.6 kcal/mol) and predicted favorable oral bioavailability, further supporting the therapeutic potential of TC2.

Beyond these findings, the current work provides a clear foundation for future research. *In vivo* validation of

TC2's efficacy and safety are a crucial next step, as are detailed mechanistic studies to elucidate its molecular targets and pathways. Additionally, further pharmacokinetic optimization could enhance its drug-likeness and support its translation into clinical applications. Overall, TC2 emerges as a promising candidate for breast cancer therapy, warranting continued investigation in preclinical and clinical settings.

CRediT authorship contribution statement

Tolga Göktürk: Investigation, Validation, Writing - Review & Editing, Turan Demircan: Methodology, Investigation, Validation, Visualization, Writing - Original Draft, Writing - Review & Editing, Tuncer Hökelek: Methodology, Formal analysis, Investigation, Visualization, Writing - Original Draft, Writing - Review & Editing, Mervenur Yavuz: Investigation, Visualization, Writing - Original Draft, Ramazan Güp: Investigation, Writing - Review & Editing, Cansu Topkaya: Conceptualization, Methodology, Investigation, Validation, Visualization, Writing - Original Draft, Writing - Review & Editing, Supervision.

Conflict of interest

The authors declare that they have no conflict of interest.

Funding

This research did not receive any specific grant from funding agencies in the public, commercial, or not-for profit sectors.

Acknowledgement

The authors acknowledge to Scientific and Technological Research Application and Research Center, Sinop University, Turkey, for the use of the Bruker APEX II QUAZAR three-circle diffractometer TH is grateful to Hacettepe University Scientific Research Project Unit (grant No. 013 D04 602 004).

Data Availability Statement

The data that supports the findings of this study are available in the supplementary material of this article.

5. References

- C. Hemmert, M. Pitié, M. Renz, H. Gornitzka, S. Soulet, B. Meunier, *J. Biol. Inorg. Chem.* 2001, 6, 14–22.
 DOI:10.1007/s007750000177
- A. M. Abu-Dief, I. M. A. Mohamed, Beni Suef Univ. J. Basic Appl. Sci. 2015, 4, 119–133. DOI:10.1016/j.bjbas.2015.05.004

- K. S. A. Melha, J. Enzyme Inhib. Med. Chem. 2008, 23, 493– 503. DOI:10.1080/14756360701631850
- 4. A. A. El-Sherif, M. R. Shehata, M. M. Shoukry, M. H. Barakat, *Spectrochim. Acta Part A Mol. Biomol. Spectrosc.* **2012**, 96, 889–897. **DOI**:10.1016/j.saa.2012.07.047
- J. L. Buss, J. Neuzil, P. Ponka, *Arch. Biochem. Biophys.* 2004, 421, 1–9. DOI:10.1016/j.abb.2003.09.044
- T. Chandrasekar, A. Arunadevi, N. Raman, J. Coord. Chem. 2021, 74, 804–822. DOI:10.1080/00958972.2020.1870967
- J. P. Costes, S. Shova, W. Wernsdorfer, *Dalton Trans.* 2008, 1843–1849. DOI:10.1039/b716098d
- 8. S. Aslam, M. Ahmad, *Benzimidazole* 2022, 27. **DOI:**10.5772/intechopen.101729
- S. R. Ibrahim, G. A. Mohamed, Phytochem. Rev. 2016, 15, 279–295. DOI:10.1007/s11101-015-9413-5
- C. Gökçe, R. Gup, J. Photochem. Photobiol. B Biol. 2013, 122, 15–23. DOI:10.1016/j.jphotobiol.2013.02.014
- G. M. Sheldrick, Acta Crystallogr. A 2015, 71, 3–8.
 DOI:10.1107/S2053273314026370
- G. M. Sheldrick, Acta Crystallogr. C 2015, 71, 3–8.
 DOI:10.1107/S2053229614024218
- L. J. Farrugia, J. Appl. Crystallogr. 2012, 45, 849–854.
 DOI:10.1107/S0021889812029111
- A. L. Spek, Acta Crystallogr. D 2009, 65, 148–155.
 DOI:10.1107/S090744490804362X
- M. Yavuz, T. Demircan, Mol. Biol. Rep. 2023, 50, 2611–2621.
 DOI:10.1007/s11033-023-08245-3
- 16. M. Yavuz, T. Demircan, *Anti-Cancer Agents Med. Chem.* **2023**, 23, 938–952. **DOI:**10.2174/1871520623666221125115542
- 17. C. Ritz, F. Baty, J. C. Streibig, D. Gerhard, *PLoS One* **2015**, *10*, e0146021. **DOI:**10.1371/journal.pone.0146021
- A. Daina, O. Michielin, V. Zoete, Sci. Rep. 2017, 7, 42717.
 DOI:10.1038/srep42717
- G. Yu, L. G. Wang, Y. Han, Q. Y. He, OMICS 2012, 16, 284–287. DOI:10.1089/omi.2011.0118
- T. Demircan, H. Hacıbektaşoğlu, M. Sibai, E. C. Fesçioğlu, E. Altuntaş, G. Öztürk, B. E. Süzek, *OMICS* 2020, 24, 370–378.
 DOI:10.1089/omi.2020.0024
- R. Kiss, M. Sandor, F. A. Szalai, J. Cheminform. 2012, 4 (Suppl 1), P17. DOI:10.1186/1758-2946-4-S1-P17
- 22. A. Grosdidier, V. Zoete, O. Michielin, *Nucleic Acids Res.* **2011**, 39, W270–W277. **DOI:**10.1093/nar/gkr366
- P. Banerjee, A. O. Eckert, A. K. Schrey, R. Preissner, *Nucleic Acids Res.* 2018, 46, W257–W263.
 DOI:10.1093/nar/gky318
- M. J. Turner, J. J. McKinnon, S. K. Wolff, D. J. Grimwood, P.R. Spackman, D. Jayatilaka, M.A. Spackman, CrystalExplorer17, The University of Western Australia.
- M. J. Turner, S. Grabowsky, D. Jayatilaka, M. A. Spackman, J. Phys. Chem. Lett. 2014, 5, 4249–4255.
 DOI:10.1021/jz502271c
- M. J. Turner, S. P. Thomas, M. W. Shi, D. Jayatilaka, M. A. Spackman, *Chem. Commun.* 2015, *51*, 3735–3738.
 DOI:10.1039/C4CC09074H
- 27. C. F. Mackenzie, P. R. Spackman, D. Jayatilaka, M. A. Spackman, *IUCrJ* **2017**, *4*, 575–587.

DOI:10.1107/S205225251700848X

- M. A. Spackman, J. J. McKinnon, D. Jayatilaka, CrystEng-Comm 2008, 10, 377–388. DOI:10.1039/b715227b
- F. L. Hirshfeld, *Theor. Chim. Acta* 1977, 44, 129–138.
 DOI:10.1007/BF00549096
- M. A. Spackman, D. Jayatilaka, CrystEngComm 2009, 11, 19–32. DOI:10.1039/B818330A
- P. Venkatesan, S. Thamotharan, A. Ilangovan, H. Liang, T. Sundius, *Spectrochim. Acta Part A* 2016, 153, 625–636.
 DOI:10.1016/j.saa.2015.09.002
- D. Jayatilaka, D. J. Grimwood, A. Lee, A. Lemay, A.J. Russel, C. Taylor, S. K. Wolff, P. Cassam-Chenai, A. Whitton, TON-TO - A System for Computational Chemistry, (2005). http:// hirshfeldsurface.net/
- 33. J. J. McKinnon, D. Jayatilaka, M. A. Spackman, Chem. Com-

- mun. 2007, 3814-3816. DOI:10.1039/b704980c
- 34. V. R. Hathwar, M. Sist, M. R. V. Jorgensen, A. H. Mamakhel, X. Wang, C. M. Hoffmann, K. Sugimoto, J. Overgaard, B. B. Iversen, *IUCrJ* **2015**, *2*, 563–574.
 - DOI:10.1107/S2052252515012130
- 35. E. Audet-Walsh, V. Giguére, *Acta Pharmacol. Sin.* **2015**, *36*, 51–61. **DOI:**10.1038/aps.2014.121
- 36. N. Ijichi, T. Shigekawa, K. Ikeda, K. Horie-Inoue, T. Fujimura, H. Tsuda, S. Inoue, *J. Steroid Biochem. Mol. Biol.* **2011**, *123*, 1–7. **DOI:**10.1016/j.jsbmb.2010.09.002
- R. B. Riggins, J. P. Lan, U. Klimach, A. Zwart, L. R. Cavalli, B.
 R. Haddad, R. Clarke, *Cancer Res.* 2008, 68, 8908–8917.
 DOI:10.1158/0008-5472.CAN-08-2669
- 38. S. Madhavan, Y. Gusev, S. Singh, R. B. Riggins, *J. Exp. Clin. Cancer Res.* **2015**, *34*, 45. **DOI**:10.1186/s13046-015-0150-9

Povzetek

Kristalno strukturo Schiffove baze 4-hidroksi-N-[(1Z)-1-(naftalen-2-il)etiliden]benzohidrazid smo določili z rentgensko difrakcijsko analizo, ki je potrdila molekulsko strukturo, predhodno izpeljano iz spektroskopskih podatkov. Molekula ima skoraj planarno razporeditev obročev. V kristalni strukturi so prisotne medmolekularne O-H···O in N-H···O vodikove vezi, ki tvorijo dvodimenzionalno mrežo, kar znatno stabilizira strukturo. Z analizo Hirshfeldove površine so bile ugotovljene ključne medmolekulske interakcije, pri čemer so pomembni H···C/C···H in H···H kontakti. Energijski izračuni nakazujejo prevladujočo vlogo elektrostatskih interakcij pri celokupni stabilizaciji kristale strukture. *In vitro* testi so pokazali pomembno protirakavo delovanje z vrednostmi IC $_{50}$ 38 μ M za celice MCF7 in 57 μ M za celice MDA-MB-231, kar kaže na od odmerka odvisno zaviranje viabilnosti celic, migracije in klonogene rasti. *In silico* analize so pokazale močno afiniteto do ERR γ in napovedale ugodno peroralno biološko uporabnost. Analiza obogatitve poti KEGG za predvidene tarče je pokazala njihovo pomembno vključenost v poti, povezane z rakom. Kombinirane strukturne, *in vitro* in *in silico* analize omogočajo celovito razumevanje lastnosti spojine, kar je dobra podlaga za prihodnje predklinične in klinične študije.

